*Article*

# CFD Investigation on Oil Injection Lubrication of Meshing Spur Gears via Lattice Boltzmann Method

**Xiaozhou Hu \*, Pengfei Li, Can Quan and Jianing Wang**

School of Mechanical and Electrical Engineering, Central South University, Changsha 410083, China
\* Correspondence: huxiaozhou@csu.edu.cn

**Abstract:** The meshless Lattice Boltzmann Method (LBM) is introduced and employed to solve the complex two-phase flow problem of jet lubrication of meshing spur gears. Computational fluid dynamics (CFD) simulations based on LBM are carried out using the model of an oil jet impacting rotating gear presented by available experiments, which reveals how the liquid column is broken throughout the tooth tip cutting off the oil jet. Typical oil flow phenomena obtained by simulations are compared with experiments, demonstrating good qualitative agreement, which validates the feasibility of LBM to simulate the air–oil–structure interaction problems involved in the jet lubrication of spur gears. A three-dimensional (3D) simulation model of a spur gear pair lubricated by an oil jet is established, and simulations with different operating conditions are conducted. The evolution process of the oil jet while injecting into the meshing zone is captured, and the effects of jet velocities, jet heights and jet angles on the lubrication performance are investigated.

**Keywords:** Lattice Boltzmann Method; jet lubrication; spur gears; flow phenomenon; oil–jet gear interaction

## 1. Introduction

Jet lubrication is primarily applied for the lubrication and cooling of high-speed gears. The rotating gears significantly affect the oil jet flow into the meshing area, which affects the lubrication and cooling performance of the high-speed gears, and can lead to insufficient lubrication or even gear scratches in the most severe cases. Nowadays, although high-speed spur gears are widely used in industrial applications, the flow mechanism of oil injection lubrication has not been fully revealed and the quantification evaluation method of jet lubrication performance is inconclusive, both of which have to be investigated further [1–3].

The investigations on oil jet lubrication are mainly conducted by experiments or CFD simulations. There is a paucity of experimental investigations on jet lubrication. Akin et al. [4] and Townsend and Akin [5] et al. presented some experimental results on the jet phenomenon of gears that revealed the influence of jet configuration parameters on the impingement depth of the spur and helical gears [6–8]. Massini [9] et al. studied the influence of gear speed on the breaking of the oil jet and the formation of the oil film on the gear surface using high-speed visualizations.

In experiments, due to the small time scale of the oil jet splash phenomenon and intensive variation in air–oil two-phase flow, high-precision measurement equipment is needed to observe the phenomena of jet impingement, oil splash, formation of droplets and oil film spreading, which is not easy to accomplish in the confined space of the gearbox. Therefore, CFD has gradually become the mainstream in the research field of oil jet lubrication, and the in-depth analyses of the oil–jet gear interaction obtained from CFD simulations even exceed those of the existing experiments [10,11].

To simulate the dramatic interaction between the oil jet and air generated by the rotating gears involved in the jet lubrication of gears, it is necessary to track the free surface between the air–oil two-phase flow. At present, a common free-surface tracking method is the Volume of Fluid method (VOF), based on which several types of research

were conducted. The VOF method discretizes the spatial domain into several fixed Euler grids, focusing on the changes in different grids over time. Yazdani and Soteriou [12] performed simulations on the engaging and disengaging conditions of rotating spur gears, and studied the thermal behavior of gears. Fondelli [13,14] et al. paid more attention to oil flow distribution, and evaluated the specific evolution and characteristics of jet impacting gears at different angles by monitoring the drag torque. Dai et al. [15–17] obtained optimal configurations of jet lubrication for meshing spur, helical and face gears based on the evaluation of the temperature distribution of the tooth surface. Wang [18] analyzed the phenomenon of jet deflection and reverse flow through CFD simulations and experiments. Wang et al. [19] and Liu et al. [20] used the oil–air ratio at meshing points and power losses as indicators to speculate on the parameter configuration for the jet injection of spur gears. Wang et al. [21] and Deshpande et al. [22] measured the pressure of the meshing point and gear temperature, respectively, and pointed out that the oil jet was directed to either the into-meshing or the out-of-meshing sides under different circumstances.

Regarding multiphase free-surface flows with large density ratios and large shear forces, the insufficient coupling of mass and momentum in the VOF method can lead to diffusion errors at the phase interface that affects the cell size at the interface [23]. Therefore, the Adaptive Mesh Refinement (AMR) method was utilized in [12–14,24] to improve grid quality and reduce errors.

As for the VOF method, how to accurately describe the gear movement is another major issue. A feasible method is to discretize the meshing process into instantaneous states to simulate separately [18,19,21]; while simulating the continuous meshing process, the center distance of the meshing gears needs to be slightly increased, which aims to ensure consistency of the grid [15–17,20]. The grid-based VOF method is associated with a fixed grid topology. The deformation of the computational domain caused by gear movement may demand the application of the following technologies, e.g., re-meshing [15–17,20], sliding interface [13,14,24] or overset approach [22]. The above correction inevitably affects the accuracy and increases the time of the calculation.

The Smoothed Particle Hydrodynamics (SPH) method has the potential to overcome the shortcomings of the above-mentioned grid-based methods. Due to its Lagrangian characteristics, the simulation does not suffer from the deformed computational domain. In addition, the inherent advection of the phase interface is independent of the interface diffusion. Keller [25,26] verified the superiority of the SPH method in the calculation time of the oil–jet gear interaction, especially single-phase SPH. However, the turbulence model is not available in SPH [27].

The Lattice Boltzmann Method (LBM) is also a type of non-grid computational CFD with Lagrangian characteristics. LBM can break through the limitations of the two CFD methods mentioned above. When LBM is used to calculate multiphase flow, there is no need to track different phase interface problems [28]; Ambrose et al. [27] proved the potential of shortening the calculation time compared with the two-phase SPH method to simulate oil jet lubrication.

At present, researchers have not reached a consensus on the indicators used to measure the lubrication performance in simulations. For different working conditions and configurations, different indicators are selected. Among them, the impingement depth [22] is easier to capture and more commonly used; the oil–air ratio near the meshing area [19,21], pressure [19,21], gear temperature [15–17,21] and power loss [20] have also been used. Moreover, Keller et al. [23] tried to propose a new measure indicator on the basis of the impingement depth after simulating the interaction between the oil jet and meshing gears.

In this work, the Lattice Boltzmann Method (LBM) is employed to simulate the oil jet lubrication of spur gears. Firstly, typical oil flow phenomena obtained by simulations are compared with experiments, which demonstrates good qualitative agreement on how the liquid column is broken throughout the tooth tip cutting off the oil jet. Then, a 3D simulation model of a spur gear pair lubricated by an oil jet is established, and the jet evolution during injection into the meshing zone is identified. Finally, the oil–air ratio of

the characteristic surface is used as an indicator to investigate the influences of different jet velocities, jet heights and jet angles on lubrication performance.

## 2. Methodology

The Lattice Boltzmann Method (LBM), a type of CFD methodology, is not based on solving discretion versions of the Navier–Stokes equations. Instead, LBM utilizes the Lattice Boltzman Equation (LBE) to deal with collision models on a lattice. This equation macroscopically discretizes flow particles on a statistical level and microscopically simplified kinetic models of flow particles.

The Lattice Boltzman Equation (LBE) essentially describes a transport process with a source term and is given by:

$$f\,(r + cdt, c + Fdt, t + dt)drdc - f\,(r,c,t)drdc = \Omega(f)drdcdt \qquad (1)$$

where $f(r,c,t)$ is the probability distribution function (PDF) of particles with the international system of units (SI) and represents the set of molecules with velocity c~c + $dc$ and position r~r + $dr$ at time $t$. $F$ is the external force acting on a molecule of unit mass. $\Omega(f)$, the collision operator, is a function with PDF as the dependent variable that shows how particles collide. The equation is simplified as follows:

$$\frac{\delta f}{\delta t} + e \cdot \nabla f = \Omega \qquad (2)$$

where $f$ is the probability distribution function (PDF), $e$ is the velocity, $\Omega$ is the collision operator. The left and right sides of the equation (above) represent the streaming and the collision terms, respectively [29].

The collision operator is generally modeled as a relaxation of the PDFs towards an equilibrium state. The model is simplified by Bhatnagar, Gross, Krook (BGK) approximation and can be written as follows [30]:

$$\Omega_i^{BGK} = \frac{1}{\tau}\left(f_i^{eq} - f_i\right) \qquad (3)$$

where $\tau$ is the relaxation time, and $f_i^{eq}$ is the local equilibrium function derived from a Maxwell–Boltzmann distribution of the pre-collision state. The process assigns macroscopic variables and ensures mass and momentum conservation.

The streaming terms define how flow particles travel through the flow domain constituted by lattice nodes. Unlike the Euler grid scheme, which is irregular and focuses on the phase interface capture of the grid, the Lagrangian lattice is strictly regular and focuses on the motion trajectories of particles. The lattice node model featured is the D3Q27, organized as an octree structure. Figure 1 shows the structure and principle of the D3Q27 model: D3 represents three-dimensional space and Q27 represents 27 velocity vectors with weight factors. Current properties at lattice nodes are up to previous properties at adjacent nodes.

After calculation of the collision and streaming terms, the macroscopic variables can be derived by calculating the statistical moment of PDF. Additionally, the Navier–Stokes equations can be derived by using a second-order Taylor expansion of streaming terms in LBE, known as the Chapman–Enskog expansion [29]. The numerical analysis of the Navier–Stokes equations is a difficult challenge due to the nonlinear nature of the behavior of fluids. The VOF method based on the Eulerian mathematical formulation of the N–S Equations is unable to deal with moving geometries and phase interfaces. Benefiting from the meshless character and Lagrange method, the above problems can be well solved with a suitable simulation environment for jet lubrication. In the Lattice Boltzmann Method, the boundary conditions provide the value for the unknown probability distribution function (PDF) of particles. Figure 2 shows, as an example, a wall boundary condition on a D2Q9 lattice scheme present from the left side. In this illustration, lattice points are shown on the left of the wall, which is used to implement the wall boundary condition. The unknown

PDFs are f1, f5 and f8, for which no incoming PDFs are available from the left side since no lattice nodes are present. Note that, depending on the wall locations and direction, the unknown PDF will change. In this example, the boundary condition will therefore impose those three distribution functions. According to different situations, different methods based on this model are applied. When the boundary moves, the assumed PDFs have corresponding velocity and kinetic energy, and the output PDFs are obtained through a series of calculations.
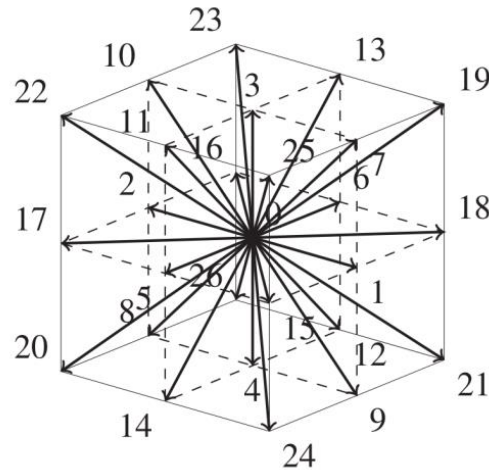


**Figure 1.** Velocity directions available from a lattice node in D3Q27 model.
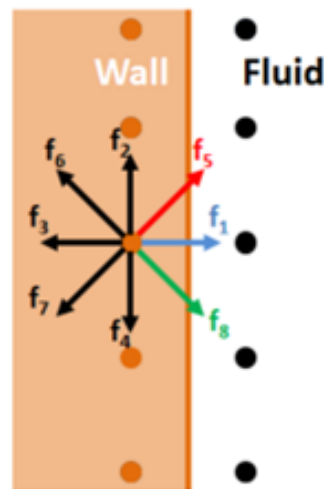


**Figure 2.** Unknown PDFs on the left wall after the streaming step.

Turbulence is modeled by an approach called Large Eddy Simulation (LES). An additional viscosity is introduced in the approach, called turbulent eddy viscosity, to model the subgrid turbulence [31]. The LES scheme in this study is the wall-adapting local eddy viscosity model (WALE). This model recovers the asymptotic behavior of the boundary layer when it can be directly solved and does not add artificial turbulent viscosity in shear regions out of the wake.

## 3. Qualitative Comparison to Experiments

### 3.1. Physical Parameters and Resolution Sets

In this paper, a qualitative comparison between flow phenomena obtained by CFD simulations based on LBM and experimental findings captured by Massini et al. [9] is performed. In Massini's work, a model describing the jet impacting a single gear was adopted. The oil jet impacted the intermediate transverse face of the gear radially. High-

speed cameras captured and recorded the formation of oil flow features such as droplets, ligaments and oil films.

The geometrical parameters of the test spur gear estimated from the given size magnitude are listed in Table 1. In this section, $L_j$ is the closest distance from the nozzle outlet to the gear pitch circle.

Three operation parameters, speed ratio, flow ratio and Weber number ratio, are given in Table 2.

The physical properties related to simulations according to calculations and reasonable assumptions are shown in Table 3.

**Table 1.** The geometrical parameters of spur gears.

| Module $m$ (mm) | Jet Diameter $D_j$ (mm) | Tooth Width $B$ (mm) | $L_j$ (mm) | Number of Teeth $Z$ |
|---|---|---|---|---|
| 4 | 1 | 55 | 75 | 38 |

**Table 2.** Operation parameters applied in simulations.

| $UR=\dfrac{U_p}{U_j}$ | $Q=\dfrac{\rho_j U_j^2}{\rho_{air} U_p^2}$ | $We_{cf}=\dfrac{\rho_{air} D_j U_p^2}{\sigma}$ |
|---|---|---|
| 1 | 875 | 2 |

**Table 3.** Physical properties used in simulations.

| $U_p(\mathrm{m\cdot s^{-1}})$ | $U_j(\mathrm{m\cdot s^{-1}})$ | $\rho_j(\mathrm{kg\cdot m^{-3}})$ | $\rho_{air}(\mathrm{kg\cdot m^{-3}})$ | $\sigma(\mathrm{N\cdot m^{-1}})$ |
|---|---|---|---|---|
| 7 | 7 | 875 | 1 | 0.025 |

ISO VG 46 was used as lubricating oil in experiments. The ambient temperature of the experiment was preset to 80 degrees Celsius and standard atmospheric pressure was adopted. In addition, the dynamic viscosity of oil and air was $1.3 \times 10^{-2}$ and $2.1 \times 10^{-5}$ Pa $\cdot$ s, respectively.

In Figure 3, some of the above physical parameters are marked, and the area covered by the shadow is the refined area that is needed to reduce the size of the lattice and enhance observation. It is only necessary to monitor the refined area to grasp the entire process of the jet impacting the spur gear, so the precision of the refined area is vital.

Concerning the mentioned physical and geometrical parameters, three sets of simulations were carried out. The dependence of the LBM model on lattice refinement was tested firstly. The detailed information of the three sets of simulations is presented in Table 4. It can be seen that three lattices of different sizes were applied to the same particle refinement region (see Figure 3), which were 1/16, 1/10 and 1/8 of the jet diameter ($D_j$), respectively. The rest of the parameters related to the calculation intensity varied accordingly. The simulations were mainly conducted on the Intel Xeon Gold 6154 or converted to the same computing resources. After weighing the simulation display and computational costs, the finest resolution of the following models in $D_j$ can be recommended.

**Table 4.** Detailed information of simulations with different lattice refinements.

| | Finest Resolution ($D_j$) | Total Number of Lattice Nodes (Million) | CPU Time for 1 Tooth Rotation (Hour) | Wall Clock Time for 1 Tooth Rotation (Hour) |
|---|---|---|---|---|
| **Model 1** | 1/16 | 54.7 | 900.3 | 45.4 |
| **Model 2** | 1/10 | 13.2 | 186.3 | 9.4 |
| **Model 3** | 1/8 | 9.4 | 156.2 | 7.9 |
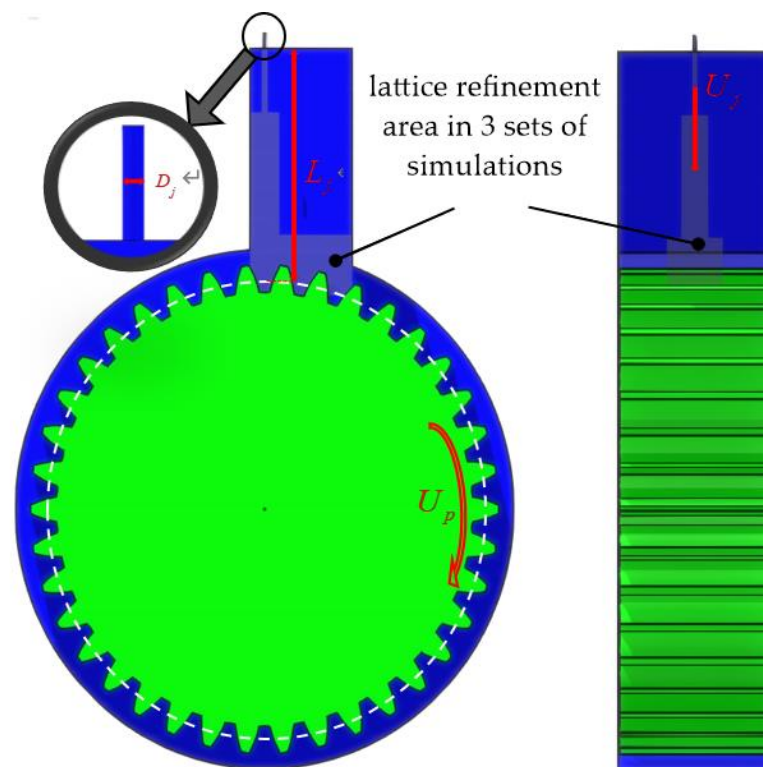
**Figure 3.** Visualization of simulation with applying test parameters.

*3.2. Results Analysis*

Figure 4 demonstrates the comparisons of lateral views between the three sets of simulations and experiments. Due to the high resolution of Model 1, the characteristics of a large number of droplets breaking up and even atomizing in the space are captured. The breakup of the jet flow hitting the tooth surface is more complicated, and it distinctly displays the ligaments of two adjacent gears. The image of Model 2 also presents a ligament similar to that of the test image, and, except for the complex jet breakup shapes, it has the basic properties of higher refinement accuracy. However, in Model 3, the connecting ligaments of the two teeth are not obvious, and the jet flow does not generate significant surface waves in the air [32].

The dark background of the experimental image in the lateral view hindered observation, so isometric views are shown in Figure 5 as a supplement. Due to the characteristics of the metal tooth surface reflecting light, the phenomenon of liquid column breakage could be more clearly captured. In Frame2, the tooth tip cuts off the jet, which forms a radial sheet; because of the effect of viscous force, the radial sheet is expanding in the circumferential direction and connecting to the bottom of the jet in Frame3; the sheet continues to extend until it impacts the adjacent flank, and forms an oil film on the flank and a ligament connecting to the original tooth tip, as shown in image Frame1.

The phenomenon and evolution of Model 1 are consistent with those of tests, and Model 2 retains the main features of Model 1, including the oil film, radial sheets and ligaments, while Model 3 loses most of the breakage details. To reduce computing costs, the refined lattice size of Model 2 is adopted in the following models, which is $D_j/10$.

From the qualitative comparison described above, it is found that LBM can well capture the various flow characteristics caused by oil–jet gear interaction in the process of jet lubrication by applying a reasonable refinement. Therefore, the feasibility and accuracy of the method used in this paper can be verified.
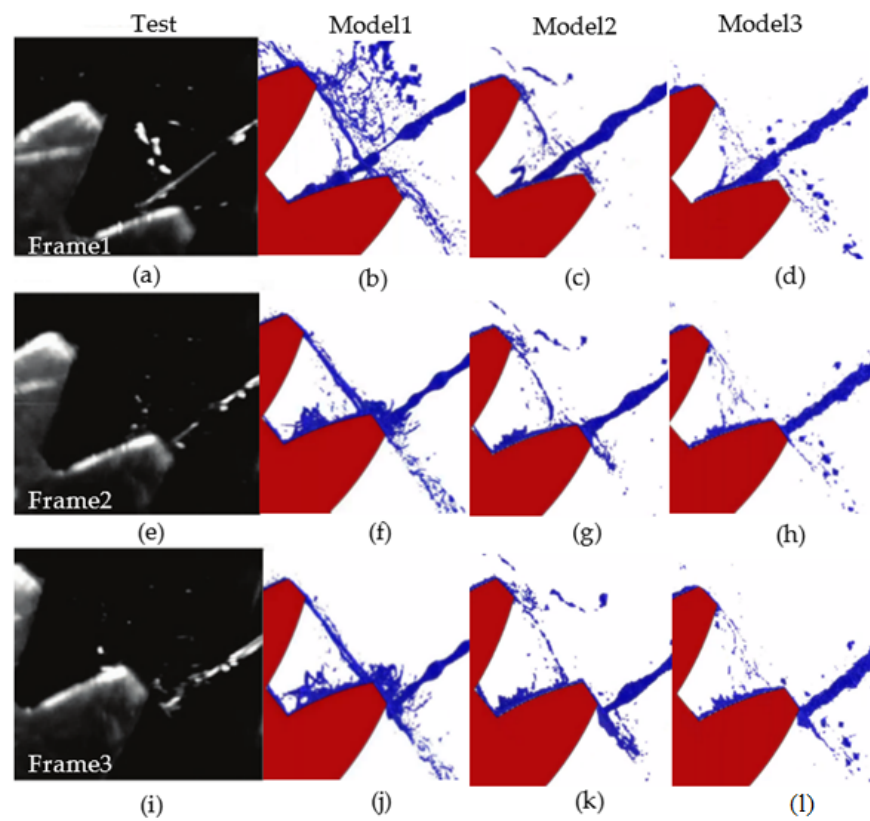
**Figure 4.** Lateral view for test or models at different frames: (**a**–**d**) test and models at Frame1; (**e**–**h**) test and models at Frame2; (**i**–**l**) test and models at Frame3.
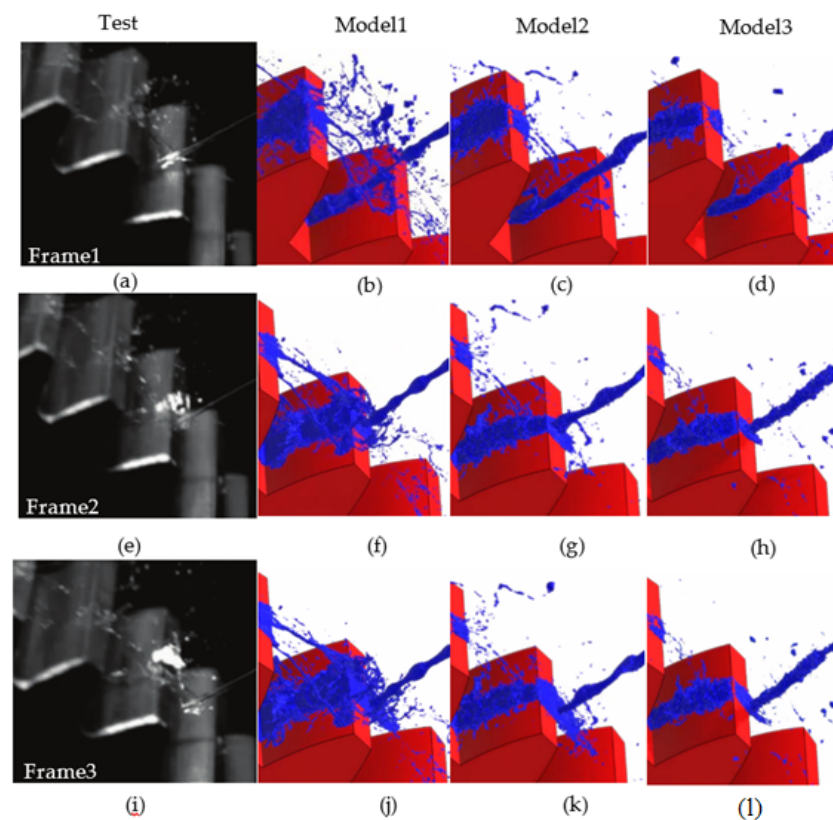


**Figure 5.** Isometric view for test or models at different frames: (**a**–**d**) test and models at Frame1; (**e**–**h**) test and models at Frame2; (**i**–**l**) test and models at Frame3.

## 4. CFD Model

### 4.1. Geometric and Physical Parameters

In view of a typical transmission system of an actual helicopter, the spur gear pair is modeled to explore the effects of the jet lubrication parameters on gear lubrication performance. The direction of the nozzle is in accordance with the common tangent of two gear pitch circles in the intermediate transverse face (see Figures 6 and 7). Table 5 shows the relevant parameters of the model.
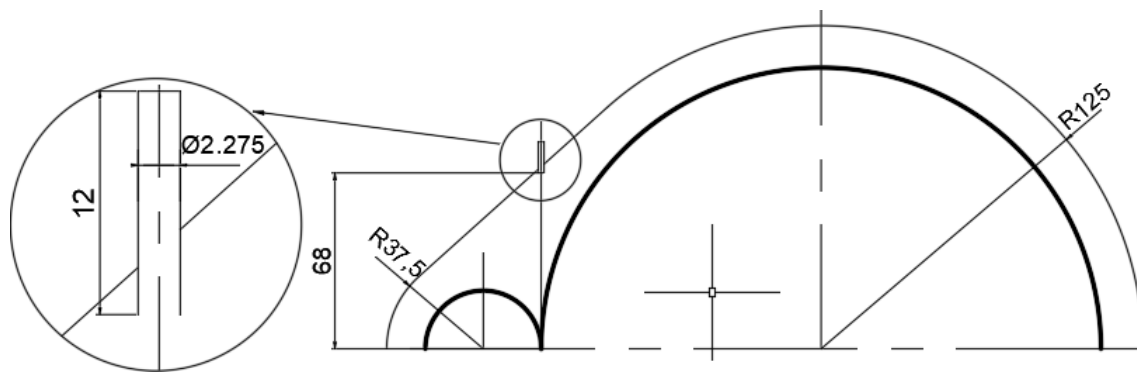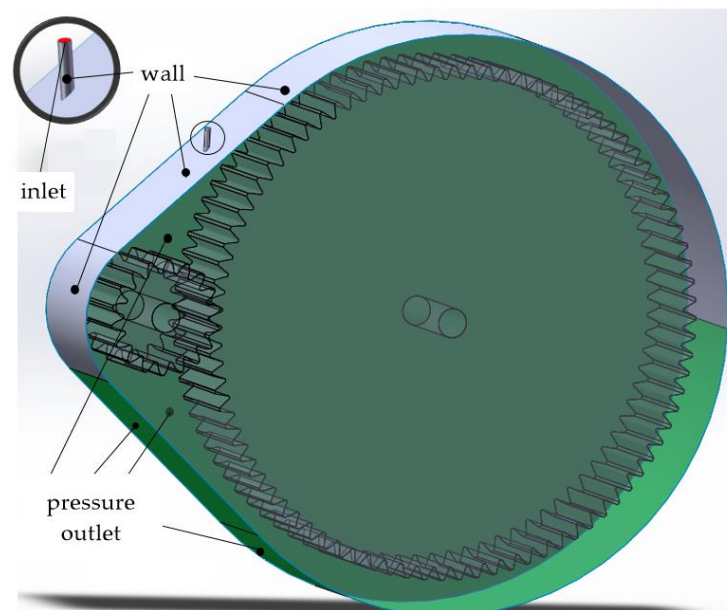


**Figure 6.** Front view of the flow domain.



**Figure 7.** BCs of the flow domain.

**Table 5.** Relevant parameters of chosen meshing gears.

|  | Module $m$ [mm] | Tooth Width $d$ [mm] | Number of Teeth $z$ | Rotational Speed $n$ [rpm] |
|---|---|---|---|---|
| **the driving wheel** | 2.5 | 45 | 18 | 29,000 |
| **the driven wheel** | 2.5 | 45 | 87 | 6000 |

According to the geometrical parameters of the gears, the three-dimensional parameters of the flow domain were determined: the width is 50 mm and the others are shown in Figure 6. Meshing spur gears are simplified as tangent pitch circles. The adiabatic model is adopted; the nozzle diameter parameter Ø is 2.275 mm, the speed inlet of the nozzle is 20 m/s, and its ratio to the gear linear speed is approximately 1:4; the overall environment is under standard atmospheric pressure; the density of oil and air are 969.6 kg/m$^3$ and

1.225 kg/m$^3$, respectively; the dynamic viscosities of oil and air are $1.12 \times 10^{-2}$ Pa·s and $1.79 \times 10^{-5}$ Pa·s, respectively.

*4.2. Boundary Conditions and Refinement Configuration*

Figure 7 shows the boundary conditions (BCs) implemented in simulations. To assume an open situation, the two sides and bottom of the flow domain are set as pressure outlets, and the gauge pressure is 0. The top surface of the nozzle is set as a velocity inlet, which can be adjusted to jets with different mass flow in simulations. Other surfaces are set as wall boundary conditions with a roughness of $1 \times 10^{-7}$ imposing the enhanced wall function, which is valid for all y+ and accurately resolves the turbulent boundary layer, taking into account the influence of curvature but disabling the pressure gradient term [33].

The behavior of the gears is adjusted to so-called "enforced", and the preset angular velocity around the axis is applied to ensure that the gears rotate around the shafts properly.

It is noted that the center distance between the two gears is increased by 0.2 mm. It can be calculated from Table 5 that the center distance of the standard meshing is 131.25 mm, but in simulations, the actual axis distance of the two gears is 131.45 mm. This modification not only avoids the high-pressure gradient caused by the closure of the meshing area between the gears, which affects the stability and convergence of the calculation, but also greatly reduces the computing cost and time. The increased value of the center distance in simulations ($D_1/225$) in this paper is much lower than those using the VOF method (approximately $D_1/30$ in [17], $D_1/20$ in [20]). Considering the elastic deformation and assembly error of the gear pair, the modification is closer to the actual working conditions.

The jet path from the nozzle to the meshing area is set as the refined area, the accuracy value of which is $D_j/10$. Moreover, the near-wall surface of the gear needs a certain degree of refinement to restore the near-wall behavior of the flow field. As shown in Figure 8, the lattice structure of a certain section is intercepted, and the blue area covered by the shadow is the refined area until gears have been engaged for a certain distance. A total of five levels of refinement and wake resolution are enabled. The total number of lattices is around 9.48 million; the total simulation time is 0.005 s, during which the pinion can rotate 2.4 times; at approximately 0.003 s, the jet enters the meshing area and participates in gear meshing, and then the two gears continue to mesh with around 16 teeth until the end of the simulation; the total wall clock time is 192.0 h with the specified stability parameter.
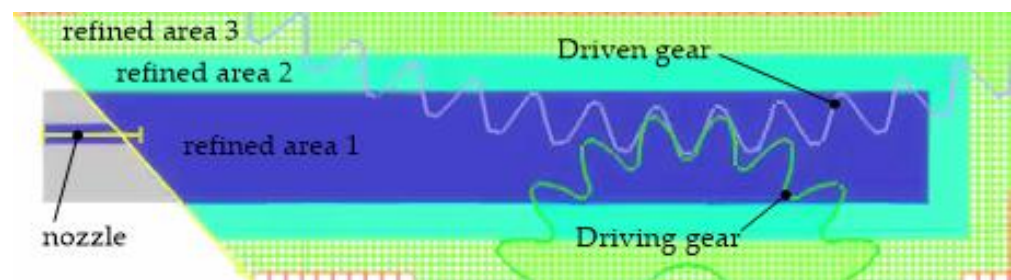


**Figure 8.** Refined lattice structure of specified section.

*4.3. The Influence of Stability Parameter in Simulations*

To some extent, the stability parameter characterizes the reliability of the calculation. With different time steps, the stability parameter of the simulation process will also fluctuate correspondingly and can be calculated as follows:

$$
\begin{aligned}
C_s &= \frac{dx}{\sqrt{3}dt} \\
S_v &= \frac{v}{C_s dx} \\
S_V &= \frac{V_{max}dt}{dx} \\
S_\rho &= \frac{2(\rho_{max} - \rho_{min})}{(\rho_{max} + \rho_{min})} \\
S &= \frac{\max(S_v, S_v, S_\rho)}{0.7}
\end{aligned}
\tag{4}
$$

where $C_s$ is the numerical speed of sound, derived from the resolution at a given lattice level $dx$ and the associated time step for the same lattice level $dt$. $S_v$ is the numerical kinematic viscosity, $v$ is the kinematic viscosity, $V_{max}$ is the local maximum speed, $S_V$ is the Courant–Friedrichs–Lewy parameter, $\rho_{max}$ and $\rho_{min}$ are the local maximum and minimum density, and $S_\rho$ is the compressibility parameter. The stability parameter must satisfy the Courant–Friedrichs–Lewy (CFL) condition as well as the compressibility and numerical viscosity conditions, and thus its value must be less than 1. The situation in which the stability parameter is more than 1 reflects the fact that the stability parameter calculation is out of balance by one or more lattices of the fluid domain (elements are highly stressed by narrow areas, geometric shape change, etc.), but it does not mean global instability.

In this paper, the stability parameter of all time steps is not strictly required to be less than 1, but the average stability parameter (ASP) of the solution time interval is controlled by around 0.6. On account of the limitation of computing time, it is impossible to completely avoid the situation wherein the stability parameter of a certain time step is more than 1, which represents the fact that the partial pressure of the fluid domain is too high at the time step. However, lubrication is used for the global space domain, and this situation is allowed to occur in a small amount in simulations.

## 5. Results and Discussion

### 5.1. Flow Phenomenon

The contour map with a VOF of 0.1 at 0.005 s is shown in Figure 9, where a, b and c are the global front view, the front view and the side view of the refinement area, respectively. In Figure 9b,c, only the image within the refined area is kept, which eliminates the observation obstacles caused by the oil film attached to gears and the droplets scattered in the space.



(a)   (b)   (c)
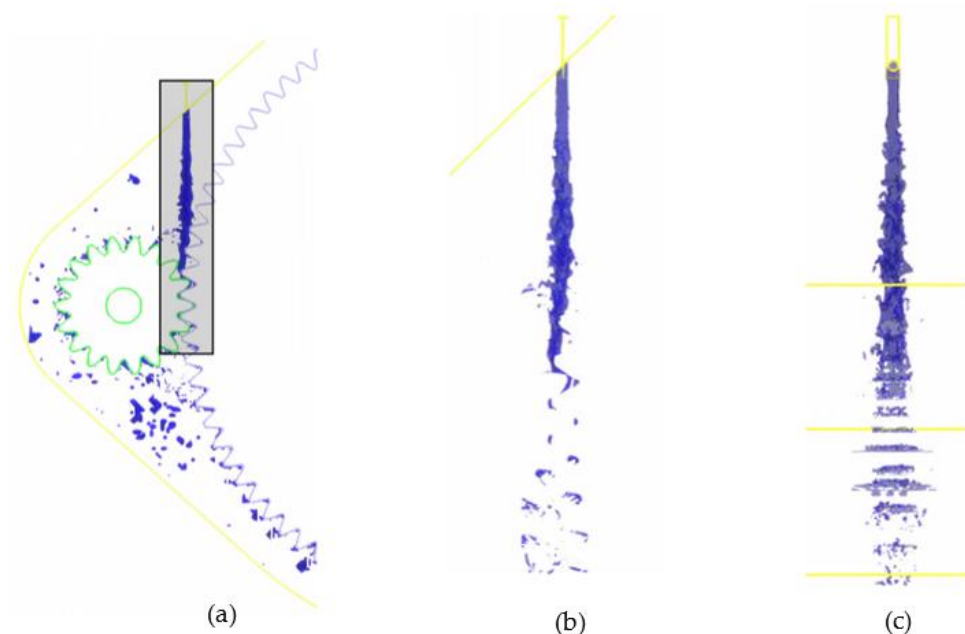
**Figure 9.** The contour map with VOF of 0.1 at 0.005 s: (**a**) global front view; (**b**) front view of the refinement area; (**c**) side view of the refinement area.

A Reynolds number between 2300 and 4000 represents the transition stage between the laminar and turbulent flow. The Reynolds number of the jet is around 3940, which can be regarded as turbulent flow. The jet in Figure 9 shows obvious turbulent properties: after being ejected from the nozzle, the jet flows forward as a whole while still pulsing randomly in all directions on the microscopic level, and it produces a strong shearing effect with the surrounding air, which reflects the gradual diffusion and turbulence of the jet on the macroscopic level.

As the jet evolves, the stream moves closer to the driven wheel, until a part of the stream collides with the gear teeth; in this process, the stream deflects slightly to the driving wheel under the high pressure near the teeth, and the pressure near the driving wheel also has an effect, so the stream narrows in the tangential direction of the gears and widens in the axial direction of the gears until it enters the meshing zone. When the current meshing is over, some droplets in the gear gap fall off into the open space under the action of inertial force and centrifugal force, and the remaining oil is still attached to the gear as a stable oil film to participate in the next meshing.

### 5.2. Analysis of Lubrication Performance
5.2.1. Lubrication Indicator

In the quantitative comparison of jet lubrication performance, one of the most often used parameters is the impingement depth [23]—that is, the radial distance of the jet penetrating the tooth gap before impinging on the tooth tip. It is usually used to measure a gear pair before meshing or a single gear without meshing. However, the backlash of standard meshing gears is small enough to be close to zero. Oil is repeatedly squeezed and compressed in the narrow area of the meshing surface, which usually causes a large amount of oil to enter the chamber formed by the clearance, as shown in Figure 9. In this situation, it is not suitable to use the impingement depth to measure the lubrication performance.

In this paper, the average oil–air ratio of the characteristic surface (OARC) is used to quantify the lubrication performance. The so-called characteristic surface is determined where the driven wheel is meshing with the driving wheel (see Figure 10) and is composed of the tooth flank and root of two adjacent teeth. OARC is a characteristic surface integral of the oil–air ratio, expressed as follows:

$$OARC = \frac{1}{A}\int_A \phi dA \qquad (5)$$

where $A$ is the area of the characteristic surface, and $\phi$ is the oil–air ratio. Quantitative comparisons of all groups are performed when the simulation proceeds to 0.005 s. When applying the parameters introduced in Section 4.1, the obtained value of OARC is 0.0145, which indicates that 1.45% of the characteristic surface area is covered by the oil film at this moment. Since the jet does not repeatedly impact the tooth surface, there is not much oil attached to the tooth surface in the situation of Section 4.1.
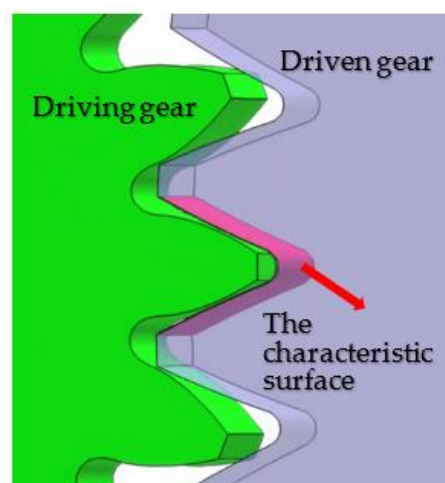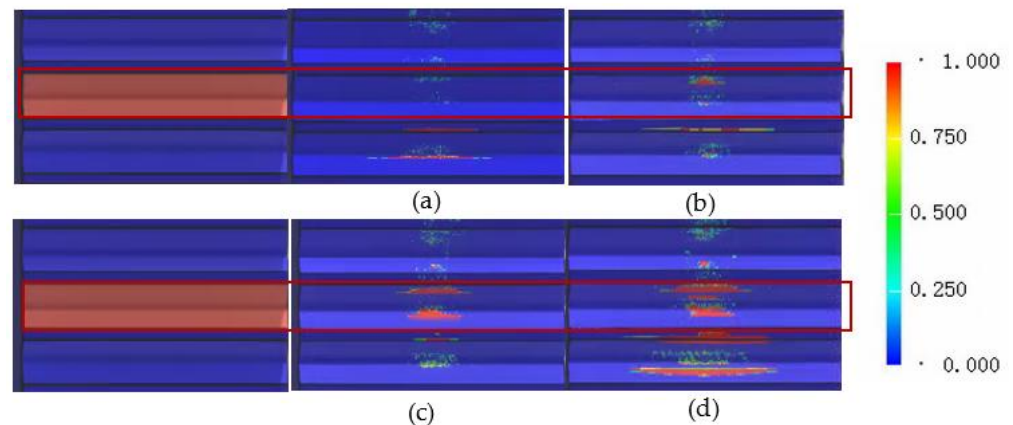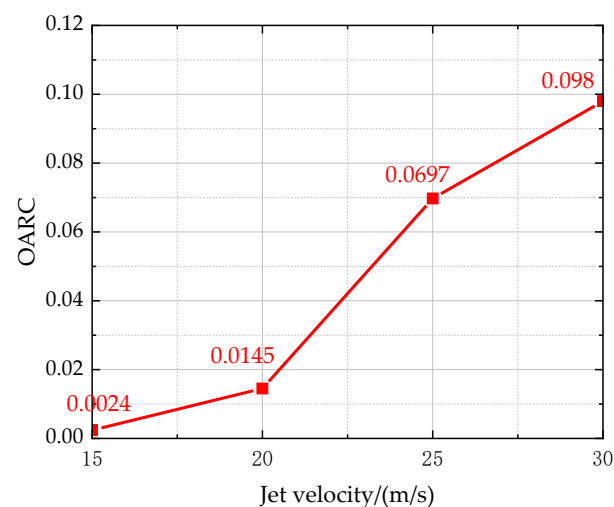


**Figure 10.** The characteristic surface.

### 5.2.2. Influence of Jet Velocities

The first group of simulations is carried out to study the influence of different jet velocities on OARC. Taking jet velocity as a variable, other parameters remain unchanged, as presented in Section 4.1. The visualized images of the oil–air ratio with different jet velocities are shown in Figure 11. The red box indicates the characteristic surface (shown in Figure 10), namely the meshing surface. Different colors indicate the different percentages of oil in the lattice on the surface of the gear tooth. The higher jet speed means a higher oil–air ratio and better lubrication performance; When the jet speed is 15 and 20 m/s, there is no or less oil accumulation on the meshing surface, which indicates that the lubrication and cooling effect may be insufficient, and the oil is quickly splashed out by the airflow. Conversely, with the higher jet speed of 25 or 30 m/s, a stable oil film can form on the tooth surface.

The calculated OARC is shown in Figure 12. Obviously, the OARC increases as the jet velocity rises. The correlation between OARC and jet velocity is nonlinear, and the slope of OARC increase is the largest from 20 to 25 m/s. When the speed reaches more than 30 m/s, the growth of the OARC tends to be gentle. This is because that jet is largely intercepted by the high-speed gear outside of the meshing zone, and the correlation between gear lubrication and speed becomes smaller.
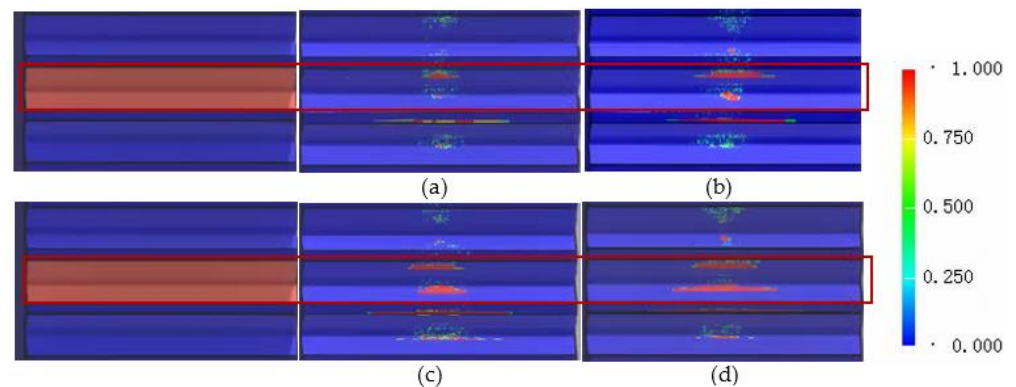


**Figure 11.** Visualized images of oil–air ratio with different jet velocities: (**a**)15 m/s; (**b**) 20 m/s; (**c**) 25 m/s; (**d**) 30 m/s.



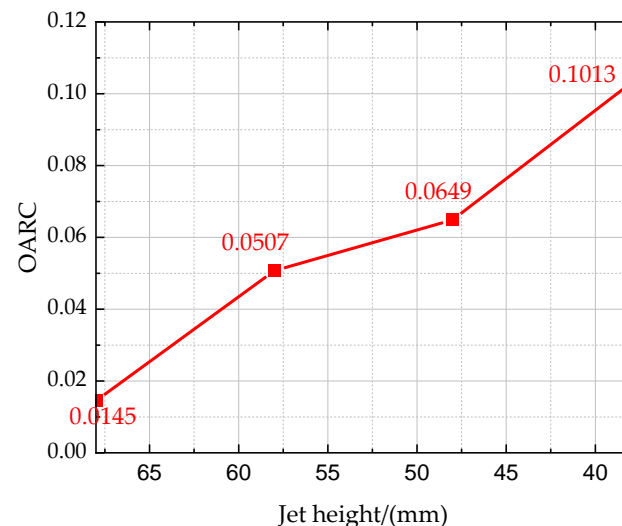**Figure 12.** OARC with different jet velocities.

### 5.2.3. Influence of Jet Heights

The second group of simulations is carried out to study the influence of different jet heights on the oil–air ratio near the characteristic surface. In this section, jet height is the closest distance from the nozzle outlet to the intersection of gear pitch circles. We take jet height as a variable and the other parameters remain unchanged, as introduced in Section 4.1. The visualized images of the oil–air ratio are shown in Figure 13. Obviously, the lower the jet height is, the higher the oil–air ratio is and the better the lubrication performance is. When the height is relatively low, the jet stays in the air for a shorter time before reaching the meshing area, and the degree of radial dispersion and deflection affected by aerodynamics are lower, and thus the jet entering the meshing gear is more concentrated; thereby, the tooth surface lubrication situation can be significantly improved.



**Figure 13.** Visualized images of oil–air ratio with different jet heights: (**a**) 68 mm; (**b**) 58 mm; (**c**) 48 mm; (**d**) 38 mm.

Figure 14 shows that the jet height is negatively correlated with the OARC. While keeping the injected mass flow constant, the area of the oil film on the gear surface can be effectively increased by eight times or more by reducing the jet height.



**Figure 14.** OARC with different jet heights.

### 5.2.4. Influence of Jet Angles

The third group of simulations is carried out to study the influence of different jet angles on the oil–air ratio. We take the jet angle as a variable, and other parameters remain unchanged, as introduced in Section 4.1. Figure 15 is a schematic diagram of different jet angles. The negative sign means that the nozzle rotates at a certain angle to the driving wheel with the intersection of the pitch circle as the axis, and vice versa.
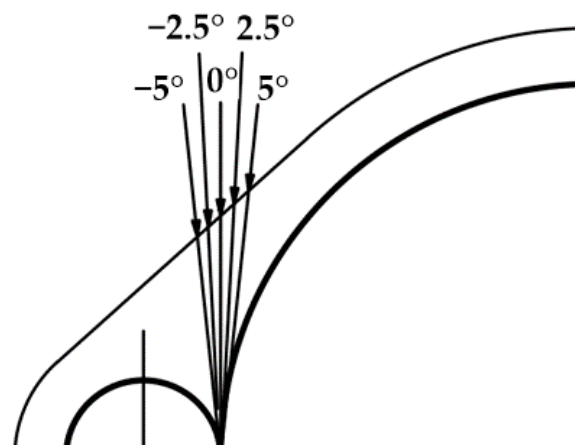
**Figure 15.** Schematic diagram of different jet angles.

Figure 16 shows the visualized images of the oil–air ratio with different jet angles. Obviously, deflection to a certain angle toward the driving wheel can significantly improve the quality of lubrication; however, if the deflection angle is too large, the lubrication performance would be reduced.
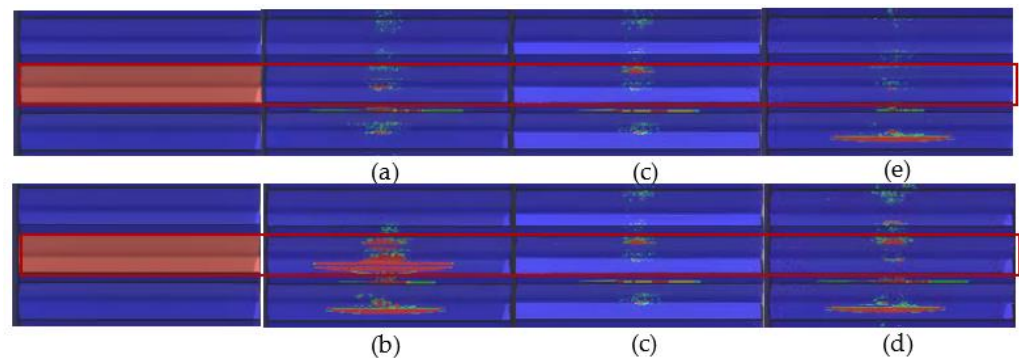


**Figure 16.** Visualization of oil–air ratio with different jet angles: (**a**) −5°; (**b**) −2.5°; (**c**) 0°; (**d**) 2.5°; (**e**) 5°.

Furthermore, the change in the oil film area of the characteristic surface caused by the deflection of the oil jet to the driven wheel is not significant. However, Figure 16d,e show that the tooth surface adjacent to and lower than the characteristic surface is covered by a large amount of oil film.

This is likely because when the jet deflects to the driven wheel, the stream collides with the top of the driven wheel earlier. A large amount of oil at the tooth top is taken into the meshing area due to inertial force and compressed into the narrow chamber of the driven wheel clearance under high pressure. Although this part of the oil participated in the first lubrication, it does not form a stable oil film on the tooth surface before meshing, so no significant increase in the oil–air ratio of the characteristic surface is observed. Then, the backlash pressure during meshing increases significantly, and it can be observed that the maximum pressure is over three times the atmospheric pressure in Figure 17. The arrow indicates the direction of the driving wheel rotation. After meshing, the narrow chamber expands to form a partial vacuum, and thus the high pressure would gradually decrease. This part of the oil will spread on the tooth surface of the driven wheel and form a stable oil film and then participate in the subsequent lubrication, followed by the oil–air ratio and visualization of the tooth surface significantly improving.
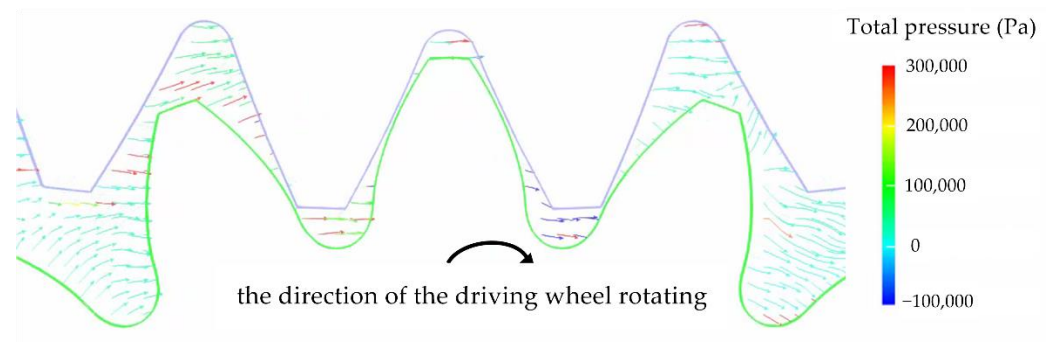
**Figure 17.** Vector view of gauge total pressure.

Figure 18 shows that a slight deflection to the driving wheel can significantly improve the lubrication, while the deflection to the driven wheel has no obvious influence on the tooth surface lubrication; however, when the deflection angle to the driving wheel or the driven wheel is too large, the lubricating effect shows a downward trend. It is suggested that the $-2.5°$ jet angle gives an ORAC one order of magnitude larger than other points. Regarding a jet angle above or below $-2.5°$, the oil jet flow is interrupted by the driving or driven gear tooth; when the jet angle is around $-2.5°$, the high-speed air flow caused by the driving gear contributes to the lubricating oil reaching the meshing region. This is consistent with the conclusion of Wang et al. [19].
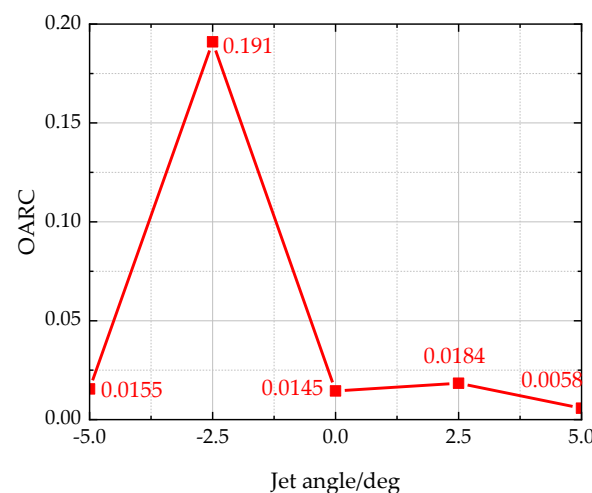


**Figure 18.** Scatter plot of OARC with different jet angles.

## 6. Conclusions

In this work, the Lattice Boltzmann Method (LBM) is employed to simulate the oil jet lubrication of meshing spur gears. The feasibility of LBM's application to simulate the oil–rotating gear interaction problems involved in the jet lubrication of spur gears is verified by qualitative comparisons between the experimental results of a single oil jet impinging on a single rotating gear and those of the corresponding simulations. The influences of different jet velocities, jet heights and jet angles on lubrication performance are investigated by CFD simulations, and the main conclusions are listed as follows:

1.  The flow phenomena obtained from simulations based on LBM are consistent with those of experiments, which reveal how the oil column is broken when being sliced by the tooth tips. By comparison with the experimental results, the optimal refinement size for simulations in this work is determined as $D_j/10$.

2.  Simulations on the oil jet lubrication of two meshing spur gears are conducted, and the jet evolution during injection into the meshing zone is identified. The gradual divergence phenomena of the turbulence in the circular tube jet into the air are analyzed.

3.　Within a certain range, a higher injection speed and lower injection height promote the movement of the lubricating oil into the meshing area, which improves the lubricating performance of the spur gear. When the lubricating oil injection velocity of the meshing gears in this paper exceeds 30 m/s, the correlation between the gear lubrication performance and the injection velocity decreases.

4.　When the nozzle is deflected towards the driving wheel by 2.5°, the lubrication performance is the best, while a small deflection towards the driven wheel has no obvious effect. However, when the deflection angle is large enough, the lubricating effect has a downward trend.

5.　In this paper, the LBM method is used to capture the various flow characteristics caused by the oil–jet gear interaction during the jet lubrication process, and the average oil–air ratio (OARC) of the characteristic surface is used to quantify the jet lubrication performance. In future work, our group will consider the effect of heat and conduct a coupled study of jet lubrication heat flow based on the LBM method. Further, the effects of different injection parameters on the gear load-independent power losses, one of the causes of gear heat generation, also will be focused on.

**Author Contributions:** Conceptualization, X.H. and C.Q.; methodology, C.Q.; software, P.L.; validation, X.H., J.W. and P.L.; formal analysis, C.Q.; investigation, P.L.; resources, X.H.; data curation, P.L.; writing—original draft preparation, C.Q.; writing—review and editing, P.L. and J.W.; visualization, C.Q.; supervision, X.H.; project administration, X.H.; funding acquisition, X.H. All authors have read and agreed to the published version of the manuscript.

**Institutional Review Board Statement:** Not applicable.

**Informed Consent Statement:** Not applicable.

**Data Availability Statement:** Data are contained within the article.

**Conflicts of Interest:** The authors declare no conflict of interest.

## References

1.　Dai, Y.; Liang, C.Y.; Chen, X.; Zhu, X. Numerical Analysis for Wetting Behaviors of an Oil Jet Lubricated Spur Gear. *Lubricants* **2022**, *10*, 17. [CrossRef]

2.　Biboulet, N.; Colin, F.; Lubrecht, A.A. Friction in starved hydrodynamically lubricated line contacts. *Tribol. Int.* **2013**, *58*, 1–6. [CrossRef]

3.　Mishra, S.P.; Polycarpou, A.A. Tribological studies of unpolished laser surface textures under starved lubrication conditions for use in air-conditioning and refrigeration compressors. *Tribol. Int.* **2011**, *44*, 1890–1901. [CrossRef]

4.　Akin, L.S.; Mross, J.J.; Townsend, D.P. Study of Lubricant Jet Flow Phenomena in Spur Gears-Out of Mesh Condition. *J. Tribol. T. ASME* **1975**, *97*, 64. [CrossRef]

5.　Townsend, D.P.; Akin, L.S. Study of Lubricant Jet Flow Phenomena in Spur Gears—Out of Mesh Condition. *J. Mec. Design* **1983**, *100*, 61–68. [CrossRef]

6.　Akin, L.S.; Townsend, D.P. Into mesh lubrication of spur gears with arbitrary offset oil jet. I—For jet velocity less than or equal to gear velocity. *J. Mec. Design* **1982**, *105*, 713–718. [CrossRef]

7.　Akin, L.S.; Townsend, D.P. Lubricant Jet Flow Phenomena in Spur and Helical Gears with Modified Addendums–for Radially Directed Individual Jets. In Proceedings of the 1989 International Power Transmission and Gearing Conference, Chicago, IL, USA, 25–28 April 1989.

8.　Akin, L.S.; Townsend, D.P. Lubricant jet flow phenomena in spur and helical gears with modified center distances and/or addendums—For out-of-mesh conditions. *J. Mech. Transm. Autom. Des.* **1985**, *107*, 24–30. [CrossRef]

9.　Massini, D.; Fondelli, T.; Facchini, B.; Tarchi, L.; Leonardi, F. High-Speed Visualizations of oil Jet Lubrication for Aero-engine Gearboxes. *Energy Procedia* **2016**, *101*, 1248–1255. [CrossRef]

10.　Liu, H.; Jurkschat, T.; Lohner, T.; Stahl, K. Detailed Investigations on the Oil Flow in Dip-Lubricated Gearboxes by the Finite Volume CFD Method. *Lubricants* **2018**, *6*, 47. [CrossRef]

11. Paggi, M.; Amicarelli, A.; Lenarda, P. SPH Modelling of Hydrodynamic Lubrication along Rough Surfaces. *Lubricants* **2019**, *7*, 103. [CrossRef]

12. Yazdani, M.; Soteriou, M.C. A novel approach for modeling the multiscale thermo-fluids of geared systems. *Int. J. Heat Mass Tran.* **2014**, *72*, 517–530. [CrossRef]

13. Fondelli, T.; Andreini, A.; Soghe, R.D.; Facchini, B.; Cipolla, L. Volume of Fluid (VOF) Analysis of Oil-Jet Lubrication for High-Speed Spur Gears Using an Adaptive Meshing Approach. In Proceedings of the ASME Turbo Expo 2015: Turbine Technical Conference and Exposition, Montreal, QC, Canada, 15–19 June 2015.

14. Fondelli, T.; Andreini, A.; Soghe, R.D.; Facchini, B.; Cipolla, L. Numerical Simulation of Oil Jet Lubrication for High Speed Gears. *Int. J. Aerosp. Eng.* **2015**, *2015*, 752457. [CrossRef]

15. Dai, Y.; Ma, F.; Zhu, X.; Su, Q.; Hu, X. Evaluation and Optimization of the Oil Jet Lubrication Performance for Orthogonal Face Gear Drive: Modelling, Simulation and Experimental Validation. *Energies* **2019**, *12*, 1935. [CrossRef]

16. Dai, Y.; Wu, W.; Zhou, H.B.; Zhang, J.; Ma, F.Y. Numerical simulation and optimization of oil jet lubrication for rotorcraft meshing gears. *Int. J. Simul. Model.* **2018**, *17*, 318–326. [CrossRef]

17. Dai, Y.; Ouyang, B.; Jia, J.; Jianeng, B. Determination of an Optimal Oil Jet Nozzle Layout for Helical Gear Lubrication: Mathematical Modeling, Numerical Simulation, and Experimental Validation. *Complexity* **2020**, *2020*, 2187027. [CrossRef]

18. Wang, Y.; Niu, W.; Song, W.; Song, G. Influence of spin flow on lubricating oil jet—Design method of oil spray parameters to high speed spur gears. *Tribol. Int.* **2015**, *92*, 290–300. [CrossRef]

19. Wang, Y.; Song, G.; Niu, W.; Chen, Y. Optimized design of spray parameters of oil jet lubricated spur gears. *Tribol. Int.* **2018**, *120*, 149–158. [CrossRef]

20. Liu, H.; Link, F.; Lohner, T.; Stahl, K. CFD Simulation of Geared Transmissions with Injection Lubrication. *Proc. Inst. Mech. Eng. Part C J. Mech. Eng. Sci.* **2018**, *233*, 7412–7422. [CrossRef]

21. Wang, Y.; Song, G.; Niu, W.; Chen, Y. Influence of oil injection methods on the lubrication process of high-speed spur gears. *Tribol. Int.* **2018**, *121*, 180–189. [CrossRef]

22. Deshpande, S.; Joshi, H.; Madhavan, J.; Mason, P.; Wink, C. Two-Way Coupled CFD Approach for Predicting Gear Temperature of Oil Jet Lubricated Transmissions. *SAE Int. J. Commer. Veh.* **2018**, *11*, 163–170. [CrossRef]

23. Zuzio, D.; Orazzo, A.; Estivalèzes, J.L.; Lagrange, I. A new efficient momentum preserving Level-Set/VOF method for high density and momentum ratio incompressible two-phase flows. *J. Comput. Phys.* **2020**, *410*, 109342. [CrossRef]

24. Keller, M.C.; Kromer, C.; Cordes, L.; Schwitzke, C.; Bauer, H.J. CFD study of oil-jet gear interaction flow phenomena in spur gears. *Aeronaut. J.* **2020**, *124*, 1301–1317. [CrossRef]

25. Keller, M.C.; Braun, S.; Wieth, L.; Chaussonnet, G.; Dauch, T.; Koch, R.; Höfler, C.; Bauer, H.-J. Numerical Modeling of Oil-Jet Lubrication for Spur Gears using Smoothed Particle Hydrodynamics. In Proceedings of the 11th International SPHERIC Workshop, Munich, Germany, 14–16 June 2016; pp. 69–76.

26. Keller, M.C.; Braun, S.; Wieth, L.; Chaussonnet, G.; Dauch, T.F.; Koch, R.; Schwitzke, C.; Bauer, H.-J. Smoothed Particle Hydrodynamics Simulation of Oil-Jet Gear Interaction. *J. Tribol.* **2019**, *141*, 071703. [CrossRef]

27. Ambrose, S.; Hervé Morvan Simmons, K. Investigation of Oil Jet Impingement on a Rotating Gear Using Lattice Boltzman Method (LBM). In Proceedings of the ASME Turbo Expo 2018: Turbomachinery Technical Conference and Exposition, Oslo, Norway, 11–15 June 2018.

28. Mohamad, A. *Lattice Boltzmann Method Fundamentals and Engineering Applications with Computer Codes*; Springer: Berlin/Heidelberg, Germany, 2011.

29. Chen, S.; Doolen, G. Lattice boltzmann methods for fluid flows. *Annu. Rev. Fluid Mech.* **1998**, *30*, 329–364. [CrossRef]

30. Bhatnagar, P.L.; Gross, E.P.; Krook, M.K. A Model for Collision Processes in Gases. I. Small Amplitude Processes in Charged and Neutral One-Component Systems. *Phys. Rev.* **1954**, *94*, 511–525. [CrossRef]

31. Weickert, M.; Teike, G.; Schmidt, O.; Sommerfeld, M. Investigation of the LES WALE turbulence model within the lattice Boltzmann framework. *Comput. Math. Appl.* **2010**, *59*, 2200–2214. [CrossRef]

32. Haenlein, A. *Disintegration of a Liquid Jet*; Technical Report Archive & Image Library: Denton, TX, USA, 1932.

33. Shih, T.H.; Povinelli, L.A.; Liu, N.S. *Application of Generalized Wall Function for Complex Turbulent Flows*; ICOMP, OAI, NASA John H Glenn Research Center: Cleveland, OH, USA, 2002.